Thin-Walled Structures 134 (2019) 395–406

Contents lists available at ScienceDirect

Thin-Walled Structures

journal homepage: www.elsevier.com/locate/tws

Full length article

Axial buckling modes and crashworthiness of circular tube with external linear gradient grooves

Ru-yang Yao[a], Guan-sheng Yin[a,*], Wen-qian Hao[b], Zhen-yu Zhao[c,d], Xuan Li[e], Xiao-li Qin[f]

[a] School of Science, Chang'an University, Xi'an 710064, China
[b] Department of Engineering Mechanics, Northwestern Polytechnical University, Xi'an 710129, China
[c] State Key Laboratory for Strength and Vibration of Mechanical Structures, Xi'an Jiaotong University, Xi'an 710049, China
[d] State Key Laboratory of Mechanics and Control of Mechanical Structures, Nanjing University of Aeronautics and Astronautics, Nanjing 210016, China
[e] CCCC Civil Engineering Science & Technology Co., Ltd., Xi'an 710075, China
[f] Modern Engineering Training Center, Chang'an University, Xi'an 710021, China

ARTICLE INFO

Keywords:
Gradient grooved tube (GGT)
Energy absorption
Buckling mode
Axial crashworthiness
Numerical simulation

ABSTRACT

Metallic circular tube with external uniform grooves has excellent behaviors on axial crashworthiness during axial compression because it can generate stable responses. In the present research, three novel energy absorbers are proposed based on uniform grooved tube (UGT), namely, depth gradient grooved tube (D-GGT), thickness gradient grooved tube (T-GGT) and coupling gradient grooved tube (C-GGT). A theoretical model considering both the depth and thickness gradients and an efficient numerical model based on axisymmetric assumption are put forward. Meanwhile, some quasi-static compression experiments are performed to validate the theoretical and numerical models. The results conclude that the deformation of gradient grooved tubes (GGTs) under axial buckling can be classified into two modes, namely, random asymptotic buckling (RAB) and sequential asymptotic buckling (SAB). Compared with UGT, the D-GGT has a slight improvement on the axial energy performance even though the sum of depth of thin-walled sections is constant; for T-GGT, a force-displacement curve with upward trend and an obvious improvement of energy absorption are observed; specially, the energy absorption characteristics of D-GGT and T-GGT will occur simultaneously when C-GGT is subjected to axial loading.

1. Introduction

Due to the excellent behaviors of energy absorbing performance and machining, thin-walled structures are widely used as energy absorbers, such as front buffer structures of vehicle, landing structures of aircraft, highway guardrail and external shells of crash cushions [1–4]. From the material point of view, the thin-walled energy absorbers can be made of metallic materials and fiber reinforced composites (FRCs) [5]. Compared with the energy absorbers made of metallic materials, the FRCs always has larger specific energy absorption (SEA) [6–10], while the deformation mechanism is more complicated [8,10–13]. Therefore, the thin-walled metallic tubular structures have attracted more and more attention in recent years because of their excellent crashworthiness and simple forms [5,14–16]. In particular, for the thin-walled metallic tubular absorbers, it has been proved that the energy dissipated by axial compression is far more than other loading conditions [1,5,10,14]. Based on rigid-plastic assumption, a theoretical model of axial buckling of circular tube was proposed by Alexander [17]. By summarizing the results of a large number of quasi-static axial compression tests, Andrews et al. [18] investigated the buckling modes of metallic circular tubes with various dimensions. According to their conclusions, the buckling modes of circular tubes under axial compression were defined as axisymmetric mode, non-axisymmetric mode, mix mode and Euler mode. Among them, the axisymmetric buckling was considered as the most desirable deformation for energy absorption. Then, based on the axisymmetric progressive buckling mode of circular tubes, a new parameter called the eccentricity factor was proposed by Wierzbicki et al. [19] and further modified by Singace et al. [20,21].

From the geometry configuration point of view, many unconventional energy absorbers have been proposed by setting cut outs [22–24], corrugates [25–29], ribs [30,31] or grooves [32–41] on the common circular tubes to regulate the axial buckling mode. As efficient unconventional energy absorbers, corrugated tubes have stable properties under axial compression [25,26]. According to different impacting velocities, the axial buckling modes of corrugated tube can be defined as dynamic asymptotic buckling, dynamic plastic bucking, and

* Corresponding author.
E-mail addresses: yaoruyang@foxmail.com (R.-y. Yao), yings@chd.edu.cn (G.-s. Yin).

https://doi.org/10.1016/j.tws.2018.10.022
Received 7 July 2018; Received in revised form 12 September 2018; Accepted 15 October 2018

transition buckling [27]. By taking the eccentricity factor and amplitude factor into account, Hao et al. [28,29] presented detailed theoretical derivations of corrugated tubes under quasi-static axial loading [28] and dynamic impacting [29]. Similarly, ribbed tubes also are a kind of unconventional energy absorbers. Axial impacting tests on a group of ribbed aluminum tubes were carried out by Adachi et al. [30] and the results showed that a critical distance between two adjacent ribs was found for generating axisymmetric or non-axisymmetric buckling mode. Moreover, Isaac et al. [31] numerically proved that the ribbed tubes had better performance under axial and oblique impacting compared with conventional circular tubes.

Compared with other unconventional tubular absorbers, grooved tubes also have excellent energy absorption performance, and easy processing is its obvious advantage [32]. An early research about the axial compression of metallic grooved tube was performed by Mamalis et al. [33], which was inspired by the axial crushing of PVC grooved tube [34]. They arranged parallel circumferential narrow grooves on the outer surface of long hollow circular tubes, and the results showed that all specimens generated the non-axisymmetric buckling mode. Hosseinipour and Daneshi [35] and Hosseinipour [36] set a series of parallel narrow grooves on both the inner and outer surfaces of circular tubes to get more stable buckling mode. Their experiment results showed that all specimens generated perfect axisymmetric collapse mode. Based on the similar structure design, Wei et al. [32] set a linear thickness gradient at the thin-walled sections and concluded that the grooved tubes with thickness gradient have better axial crashworthiness than uniform ones. There are two typical features of the grooved tubes given in previous researches [32–36]: one is that both the thin-walled sections and thick-walled sections of a tube participate in energy absorption; the other is that each thin-walled section is too narrow to generate a fold. Therefore, "Type A" grooved tube is defined in this research. Actually, there exists another type of grooved tubes, which is defined as "Type B". The "Type B" grooved tube also has two typical features, namely, the folds just occur at the thin-walled sections because each of them has enough width to generate a fold, and the thick-walled sections are just used to keep the tube stable during axial compression. For the "Type B" grooved tubes, circular tubes with external parallel wide grooves under axial quasi-static compression were investigated by Salehghaffari et al. [37] and Mokhtarnezhad et al. [38] experimentally. Additionally, both single and multi-objective design optimization for grooved tubes was also carried out by Salehghaffari et al. [39]. To take foam filling into account, low velocity impacting tests were conducted by Darvizeh et al. [40]. The results showed that the axial crashworthiness under quasi-static and dynamic loading of the grooved tube was improved significantly by foam filling.

According to the conclusions of previous researches on "Type B" grooved tubes [37–40], the axisymmetric folds always generate at their thin-walled sections. However, the depth and thickness of thin-walled sections are set uniformly along the axial direction of these tubes, which may result in randomness of folding sequence. Additionally, in the process of manufacturing thin-walled tubular components with machine tools, the roundness, surface roughness and verticality may have a great influence on the experiment results. Many obvious surface chatter marks or rust are observed on the surfaces of specimens of Salehghaffari et al. [37], Mokhtarnezhad et al. [38] and Darvizeh, et al. [40] before axial compression test, which may lead to some unexpected effects on the conclusions. From the simulation point of view, three-dimensional numerical modeling method is most commonly used for both of the "Type A" and "Type B" grooved tubes. Nevertheless, this method may not take care of the computation time and precision simultaneously because enough solid elements must be required along the shell thickness [32,38,39,41]. That is to say, excessive number of elements makes larger rounding error and longer computation time, but too little number will cause lower accuracy and unnecessary hourglass deformation.

In the present research, the influences of depth gradient, thickness gradient and coupling gradient of thin-walled sections on the axial crushing behaviors of "type B" grooved tube have been investigated. A novel relational expression between axial crashworthiness parameters (in Section 2.2.4) and dimensional parameters (depth gradient, thickness gradient, depth of thin-walled section and thick-walled section, etc.) are proposed based on energy conservation principle in the theoretical model. Furthermore, some quasi-static experiments are carried out, and a novel numerical model for grooved tube with high efficiency is established by ABAQUS software to expand samples. This study aims to investigate the buckling modes and energy absorbing characteristics of depth gradient grooved tube (D-GGT), thickness gradient grooved tube (T-GGT) and coupling gradient grooved tube (C-GGT) under axial crushing. The conclusions obtained from this research will give a reference to the studies of gradient grooved tube (GGT) subjected to axial compressed.

2. Theoretical model

2.1. Basic geometric relations

The diagram of circular tube cutting by external gradient grooves is shown in Fig. 1a. The cylinder at a groove is called a thin-walled section and the part between two adjacent thin-walled sections is called a thick-walled thin-walled section. The depth and thickness of thin-walled

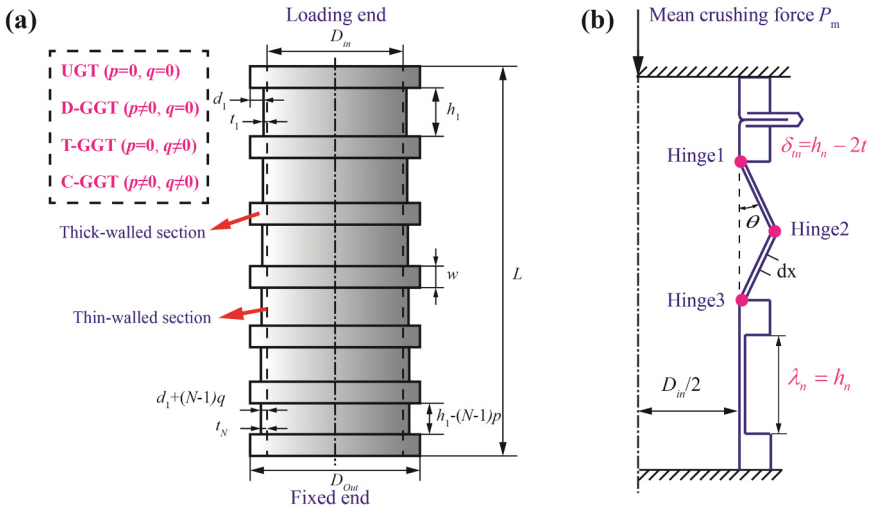

Fig. 1. Geometric and theoretical model of gradient grooved tube (GGT): (a) geometric model; (b) theoretical model [38,39].

Table 1
Parameters required of all conditions.

No. of grooves	L (mm)	D_{out} (mm)	D_{in} (mm)	w (mm)			t_1 (mm)			p (mm)			q (mm)		
				$w^{(1)}$	$w^{(2)}$	$w^{(3)}$	$t_1^{(1)}$	$t_1^{(2)}$	$t_1^{(3)}$	$p^{(1)}$	$p^{(2)}$	$p^{(3)}$	$q^{(1)}$	$q^{(2)}$	$q^{(3)}$
6	146	63	55	6.5	7.25	8	1	1.3	1.6	0	1	2	0	0.1	0.2

Note: the brackets in the superscript of parameters indicate the number of conditions.

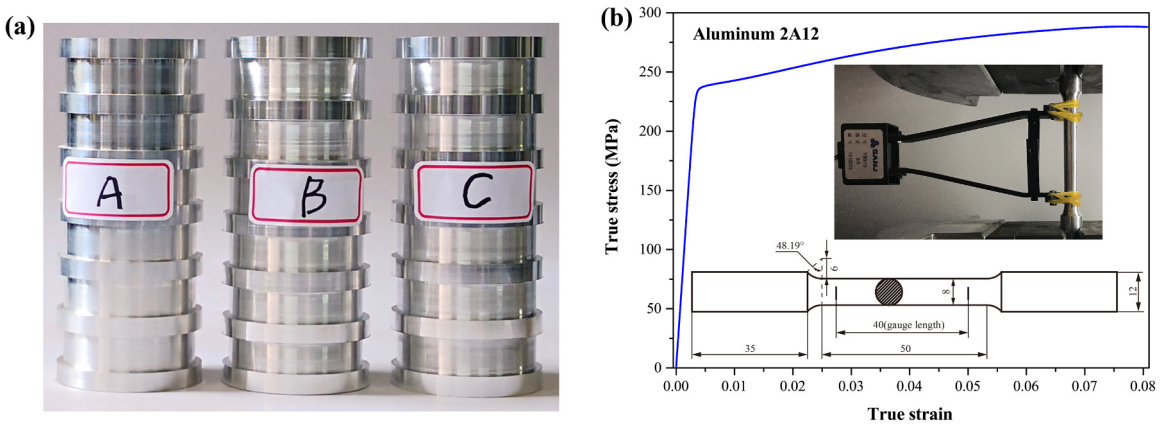

Fig. 2. Experimental works for GGTs and material properties: (a) machined specimens for quasi-static experiments (A, B and C represent conditions ($w^{(3)}$, $t_1^{(1)}$, $p^{(1)}$, $q^{(1)}$), ($w^{(3)}$, $t_1^{(1)}$, $p^{(2)}$, $q^{(1)}$) and ($w^{(3)}$, $t_1^{(1)}$, $p^{(1)}$, $q^{(2)}$), respectively); (b) true stress–strain curve of aluminum 2A12.

Table 2
Material parameters of aluminum 2A12.

Material	Young's modulus E (GPa)	Density ρ(kg/mm^3)	Yield stress σ_y (MPa)	Ultimate tensile stress σ_u (MPa)	Poisson's ratio μ
Aluminum 2A12	73	2.65×10^{-6}	235.65	288.01	0.3

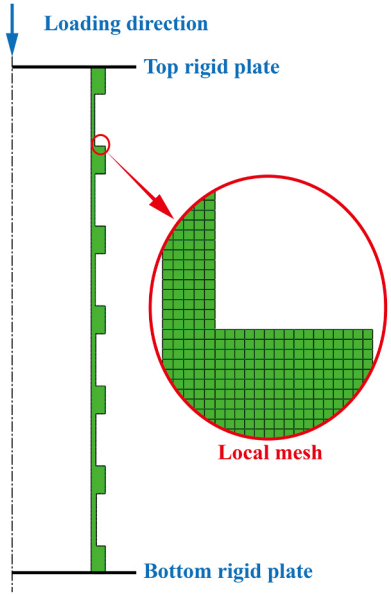

Fig. 3. Typical numerical model under condition ($w^{(3)}$, $t_1^{(1)}$, $p^{(1)}$, $q^{(2)}$) with 8605 CAX4R elements and 40 RAX2 elements.

sections show linear change along the axial direction of tube, and the deepest and thinnest thin-walled section is arranged near the loading end. According to Fig. 1a, h_n and t_n are the depth and thickness of the nth thin-walled section, respectively, and the expressions are described as following

$$h_n = h_1 - (n-1)p,\ p \geq 0 \tag{1a}$$

$$t_n = t_1 + (n-1)q,\ q \geq 0 \tag{1b}$$

where h_1 and t_1 are the initial depth and thickness of the thin-walled section at the loading end, respectively. p and q are the depth gradient, thickness gradient, respectively. $n = 1, 2, \ldots, N$ is the location number of grooves (thin-walled section), where N is the number of groove (thin-walled section), and $n = 1$ means the groove (thin-walled section) near the loading end. In the present research, the tube's outside diameter D_{out}, inside diameter D_{in}, length L and N are held fixed, while the other geometric parameters are allow to vary. The geometric relation between the thin-walled section and thick-walled section along the axial direction of tube is given by

$$(N+1)w + \frac{(h_1 + h_N)N}{2} = L \tag{2}$$

where w is the depth of thick-walled section. The first term of the left side of Eq. (2) represents the total depth of thick-walled sections, while second term represents the total depth of thin-walled sections. Additionally, because the grooved tube is machined by cutting grooves on the outer surface of a thick-walled circular tube, the geometric relation between the thickness of thick-walled sections and thin-walled sections can be expressed as

$$(D_{out} - D_{in})/2 = d_n + t_n \tag{3}$$

where d_n is the width of the nth groove. According to the geometric parameters and the material density ρ, the total mass of a GGT is given by

$$M = \frac{w\pi\rho(N+1)}{4}(D_{out}^2 - D_{in}^2) + \sum_{n=1}^{N} t_n h_n \pi D_n \rho \tag{4}$$

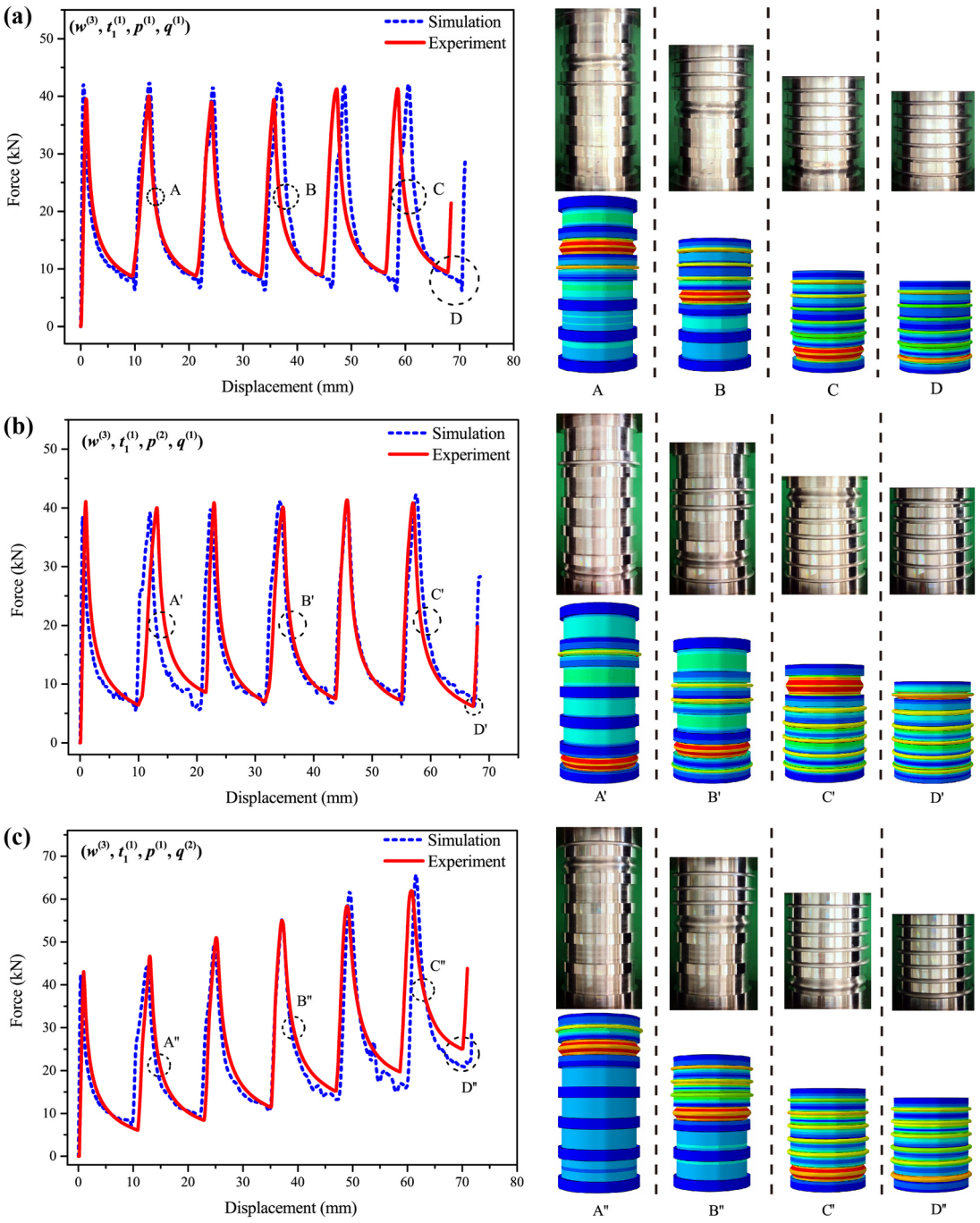

Fig. 4. Force-displacement curves and buckling modes of experiment and numerical results: (a) random asymptotic buckling (RAB) ($w^{(3)}$, $t_1^{(1)}$, $p^{(1)}$, $q^{(1)}$); (b) random asymptotic buckling (RAB) ($w^{(3)}$, $t_1^{(1)}$, $p^{(2)}$, $q^{(1)}$); sequential asymptotic buckling (SAB)($w^{(3)}$, $t_1^{(1)}$, $p^{(1)}$, $q^{(2)}$).

where D_n is the mean diameter of the nth thin-walled section and described as follow

$$D_n = D_{in} + t_n \tag{5}$$

Based on the findings of Salehghaffari et al. [37,39], the grooved tube is more likely to generate stable axisymmetric folds at it thin-walled sections when $h_n/w \le 11.8$, $0.25 \le t_n/(t_n + d_n) \le 0.8$ and $1.2 \le w/(t_n + d_n) \le 6.8$. Therefore, the external dimensions of the tube that we chose are as follows: $L = 146$ mm, $D_{in} = 55$ mm, $D_{out} = 63$ mm, $N = 6$. The arrangement and design of the gradient grooves are listed in Table 1, all conditions designed in this research are assumed to generate the stable axisymmetric buckling.

2.2. Theoretical analysis

2.2.1. Mechanisms and assumptions of plastic buckling

Based on a plastic hinge mechanism developed by Alexander [17] and Salehghaffari et al. [38,39], a theoretical model considering the depth and thickness gradient of thin-walled sections is set up for GGT. According to Fig. 1b, three stationary plastic hinges (hinge 1, hinge 2 and hinge 3) generate at each thin-walled section. The stress field in the GGT can be treated as a plane stress ($\sigma_x \neq 0$, $\sigma_\theta \neq 0$) because of neglecting the stresses σ_z, τ_{yz} and τ_{xz} [19]. Based on energy conservation principle, the total work done by external force W_T is dissipated by bending and stretching energy in the process of axial crushing. Therefore

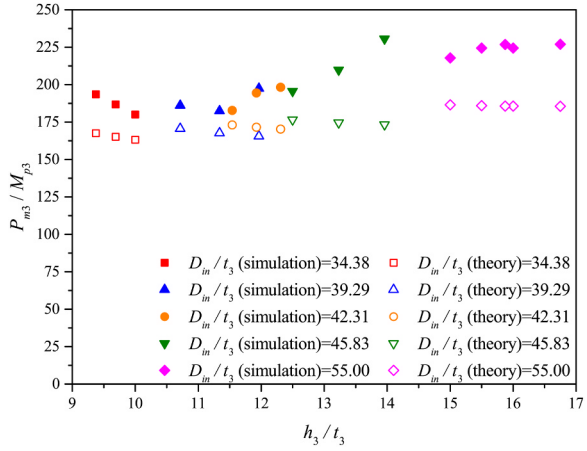

Fig. 5. Comparisons of theory results with simulation results of the third thin-walled section (n = 3) under all loading conditions.

$$W_T = P_m \cdot \delta_T = E_B + E_E = \sum_{n=1}^{N} (E_{bn} + E_{en}) \tag{6}$$

where P_m is the mean crushing force, δ_T is the total compression displacement. E_B and E_E are the energy dissipated by bending and stretching of the whole tube, respectively. E_{bn} and E_{en} are the energy dissipated by bending and stretching of the nth thin-walled section.

In addition, some assumptions about this analytical model must be explained as follows.

(a) The elastic strain is ignored (rigid-plastic material model is used), because the plastic behaviors of material play a dominant role in the large deformation [1].

(b) According to theoretical model proposed by Mokhtarnezhad et al. [38], the axisymmetric folds only generate at the thin-walled sections of grooved tube, and each thin-walled section can form just one fold. Additionally, the wavelength of a fold λ_n is equal to the corresponding h_n (Fig. 1b). It can be analyzed from the previous researches about "Type B" grooved tube [37–40] that the h_n is smaller than the inherent wavelength ($2\sqrt{D_n t_n}$) of a circular tube [17,19,20,32], while the minimum depth of the thin-walled section to form a complete fold must be measured by experiment or simulation.

(c) Based on the assumptions of Alexander [17], the contributions of bending and stretching are considered independently and all frictions are ignored. Additionally, the thickness of each thin-walled section will not change in the process of folding.

2.2.2. The energy dissipated by bending

During an increment of $d\theta$ of the angle θ, the energy dissipated by the rotation of the hinge 1 or 3 of the nth thin-walled section is given by

$$E_{bn}^{\mathrm{I}} = \pi D_n \int_{\theta} M_{pn} d\theta \tag{7}$$

Similarly, the energy dissipated by the rotation of the hinge 2 of the nth thin-walled section becomes

$$E_{bn}^{\mathrm{II}} = 2\pi \int_{\theta} (D_n + h_n \sin\theta) M_{pn} \mathrm{d}\theta \tag{8}$$

where M_{pn} is the plastic limit bending moment per unit circumferential of the nth thin-walled section by using Von Mises criterion, and it can be expressed as

$$M_{pn} = \frac{t_n^2}{2\sqrt{3}}\sigma_0 = \frac{(t_1 + (n-1)q)^2\sigma_0}{2\sqrt{3}} \tag{9}$$

where σ_0 is the flow stress. To account for stress hardening effects, σ_0 is expressed as

$$\sigma_0 = \frac{(\sigma_y + \sigma_u)}{2} \tag{10}$$

where σ_y and σ_u are the yield stress and ultimate tensile stress of material, respectively.

Combining Eqs. (7) and (8), when the θ changes from 0 to $\pi/2$, the energy dissipated by bending of the nth thin-walled section is given by

$$E_{bn} = 2E_{bn}^{\mathrm{I}} + E_{bn}^{\mathrm{II}} = 2\pi M_{pn}(\pi D_n + h_n) \tag{11}$$

The Eq. (11) is consistent with the theory result concluded by Mokhtarnezhad et al. [38].

2.2.3. The energy dissipated by stretching

For the nth thin-walled section, the tensile strain energy increment of materials between two adjacent plastic hinges can be expressed as

$$dE_{en} = \sigma_0 \varepsilon_{en} dV_{en} \tag{12}$$

where ε_{en} and V_{en} are the mean tensile strain and the volume between two adjacent hinges of the nth thin-walled section. when $\theta = \pi/2$ and the large deformation effects are considered, the ε_{en} is written approximately by

$$\varepsilon_{en} = \ln\left(\frac{D_n + 2x\sin\theta}{D_n}\right) \approx \frac{2x}{D_n} \tag{13}$$

where x is the stretch deformation distance between 0 and $h_n/2$. The differential of the V_{en} is given by

$$dV_{en} = \pi D_n t_n dx \tag{14}$$

Combining Eqs. (12)–(14), when the x changes from 0 to $h_n/2$, the energy dissipated by stretching of the nth thin-walled section is expressed as

$$E_{en} = 2\int_{\Omega} dE_{en} = 2\int_0^{\frac{h_n}{2}} \pi D_n t_n \sigma_0 \ln\left(\frac{D_n + 2x\sin\theta}{D_n}\right) dx = \frac{\pi t_n \sigma_0 h_n^2}{2} \tag{15}$$

As GGT is degenerated into the uniform grooved tube (UGT), the Eq. (15) is consistent with the theory result obtained by Mokhtarnezhad et al. [38].

2.2.4. Crashworthiness parameters

In this research, four crashworthiness parameters are employed to evaluate the axial performance of GGT, including the total energy absorption (E_T) [39], specific energy absorption (SEA) [42], stroke

Table 3
Comparisons of the experiment, simulation and theory results of axial crashworthiness parameters under conditions ($w^{(3)}$, $t_1^{(1)}$, $p^{(1)}$, $q^{(1)}$), ($w^{(3)}$, $t_1^{(1)}$, $p^{(2)}$, $q^{(1)}$) and($w^{(3)}$, $t_1^{(1)}$, $p^{(1)}$, $q^{(2)}$).

Condition	E_T (J)			P_m (kN)			SEA (J/kg)			SE		
	Exp.	Simul.	Theo.	Exp.	Simul.	Theo.	Exp.	Simul.	Theo.	Exp.	Simul.	Theo.
($w^{(3)}$, $t_1^{(1)}$, $p^{(1)}$, $q^{(1)}$)	1143.16	1161.84	1143.16	16.87	16.46	14.64	7.56	7.68	7.51	46.41	48.34	53.42
($w^{(3)}$, $t_1^{(1)}$, $p^{(2)}$, $q^{(1)}$)	1148.87	1163.17	1149.21	17.09	16.79	14.73	7.60	7.69	7.56	46.05	47.45	53.42
($w^{(3)}$, $t_1^{(1)}$, $p^{(1)}$, $q^{(2)}$)	1714.39	1678.26	1632.18	24.48	23.45	21.76	10.54	10.39	10.03	47.97	49.07	51.37

Table 4
Buckling modes of depth gradient conditions obtained by simulation results.

Parameter (mm, mm, mm, mm)	Buckling Mode	Parameter (mm, mm, mm, mm)	Buckling Mode	Parameter (mm, mm, mm, mm)	Buckling Mode
$(w^{(3)}, t_1^{(1)}, p^{(1)}, q^{(1)})$	RAB	$(w^{(3)}, t_1^{(2)}, p^{(1)}, q^{(1)})$	RAB	$(w^{(3)}, t_1^{(3)}, p^{(1)}, q^{(1)})$	RAB
$(w^{(3)}, t_1^{(1)}, p^{(2)}, q^{(1)})$	RAB	$(w^{(3)}, t_1^{(2)}, p^{(2)}, q^{(1)})$	RAB	$(w^{(3)}, t_1^{(3)}, p^{(2)}, q^{(1)})$	RAB
$(w^{(3)}, t_1^{(1)}, p^{(3)}, q^{(1)})$	RAB	$(w^{(3)}, t_1^{(2)}, p^{(3)}, q^{(1)})$	RAB	$(w^{(3)}, t_1^{(3)}, p^{(3)}, q^{(1)})$	RAB

Note: the condition of $p = 0$ mm is viewed as a special type of depth gradient tube.

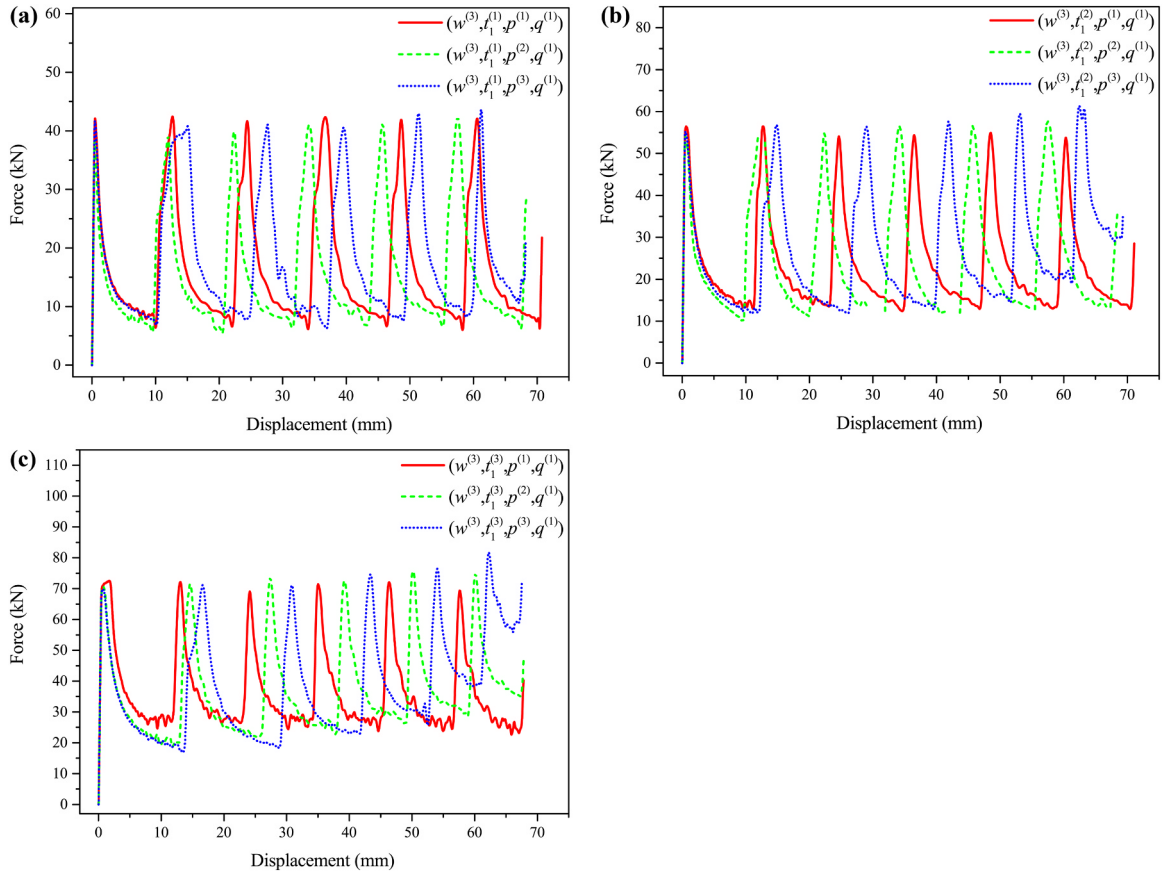

Fig. 6. Typical force-displacement curves of depth gradient conditions obtained by simulation results: (a) $t_1 = 1$ mm; (b) $t_1 = 1.3$mm; (c) $t_1 = 1.6$mm.

efficiency (*SE*) [43] and mean crushing force (P_m) [44].

According to Eq. (11) and (15), the energy absorption of the *n*th thin-walled section is

$$E_{tn} = E_{bn} + E_{en} = \pi t_n^2 \sigma_0 \left(\frac{\pi D_n + h_n}{\sqrt{3}} + \frac{h_n^2}{2t_n} \right) \tag{16}$$

From Eq. (6) and (16), the total energy absorption of whole tube can be obtained by

$$E_T = \sum_{n=1}^{N} E_{tn} = \sum_{n=1}^{N} \pi t_n^2 \sigma_0 \left(\frac{\pi D_n + h_n}{\sqrt{3}} + \frac{h_n^2}{2t_n} \right) \tag{17}$$

The specific energy is defined as a ratio of the E_T to the M of GGT and this value is hoped to as large as possible. According to Eq. (4) and (17), the *SEA* is calculated by

$$SEA = \frac{E_T}{M} = \frac{4 \sum_{n=1}^{N} t_n^2 \sigma_0 \left(\frac{\pi D_n + h_n}{\sqrt{3}} + \frac{h_n^2}{2t_n} \right)}{w\rho(N+1)(D_{out}^2 - D_{in}^2) + 4 \sum_{n=1}^{N} t_n h_n D_n \rho} \tag{18}$$

The stroke efficiency is defined as a ratio of the total compression displacement to the tube length. The *SE* is expected to have a larger value, the expression can be written as follow

$$SE = \frac{\delta_T}{L} = \frac{\sum_{n=1}^{N} \delta_{tn}}{L} \tag{19}$$

where δ_{tn} is the compression displacement of the *n*th thin-walled section. According to the assumption (b) in Section 2.2.1, the δ_{tn} can be defined as

$$\delta_{tn} = h_n - 2t_n \tag{20}$$

As a significant parameter, the mean crushing force of GGT is given by

$$P_m = \frac{E_T}{\delta_T} = \frac{\sum_{n=1}^{N} \pi t_n^2 \sigma_0 \left(\frac{\pi D_n + h_n}{\sqrt{3}} + \frac{h_n^2}{2t_n} \right)}{\sum_{n=1}^{N} (h_n - 2t_n)} \tag{21}$$

Similarly, the mean crushing force of the *n*th thin-walled section is given by

$$P_{mn} = \frac{E_{tn}}{\delta_{tn}} = \frac{\pi t_n^2 \sigma_0 \left(\frac{\pi D_n + h_n}{\sqrt{3}} + \frac{h_n^2}{2t_n} \right)}{(h_n - 2t_n)} \tag{22}$$

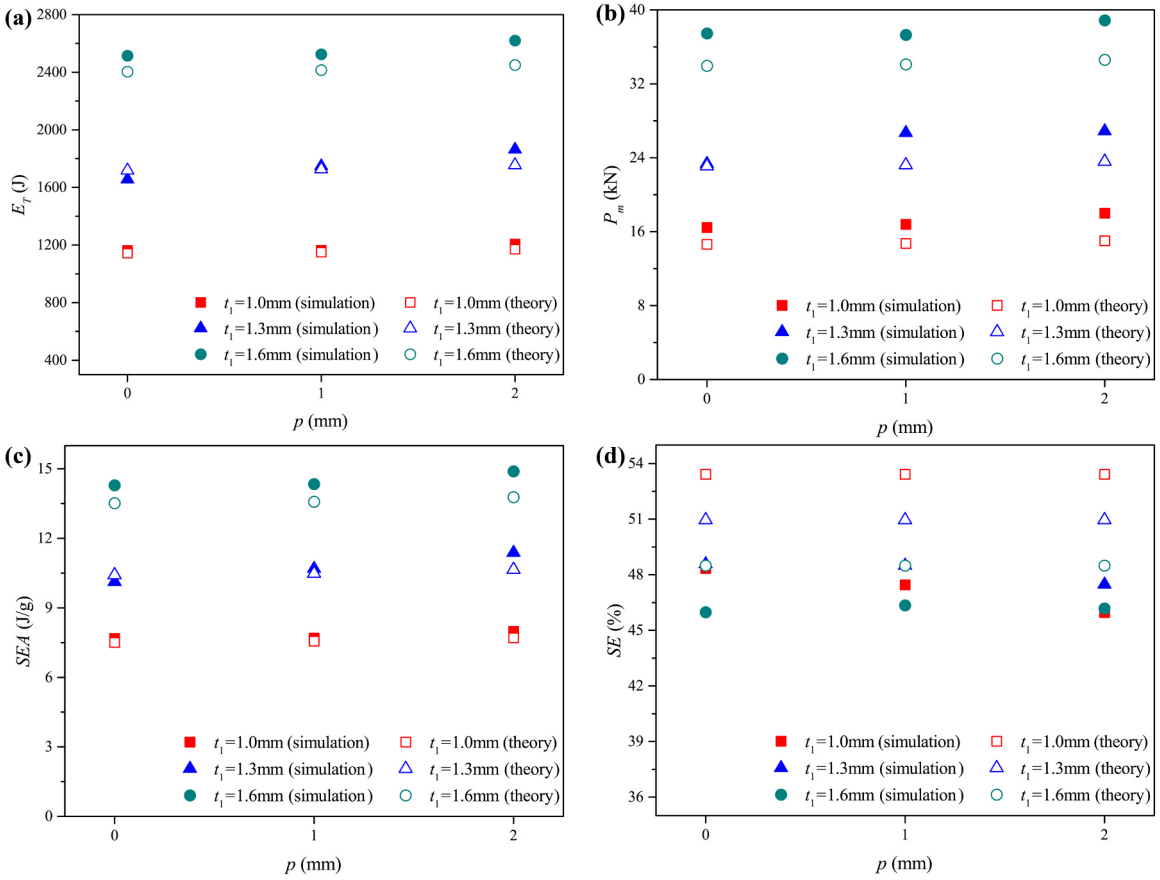

Fig. 7. The simulation and theory results of axial crashworthiness parameters under depth gradient conditions: (a) E_T; (b) P_m; (c) *SEA*; (d) *SE*.

According to Eq. (9) and (22), the normalized mean crushing force of the *n*th thin-walled section can be obtained by

$$\frac{P_{mn}}{M_{pn}} = \frac{\pi\left(\sqrt{3}\frac{h_n^2}{t_n^2} + 2\frac{h_n}{t_n} + 2\pi\frac{D_{in}}{t_n} + 2\pi\right)}{\frac{h_n}{t_n} - 2} \tag{23}$$

3. Experiment

3.1. Experimental preparation of grooved tubes

A long seamless aluminum 2A12 circular tube with an external diameter of 66 mm and an internal diameter of 38 mm was used to machine for the required conditions and "dog-bone" specimens. To minimize the machining errors, the dimensional tolerances of all specimens were limited to ± 0.01 mm, and all their surface areas were polished carefully. The machined specimens under condition $(w^{(3)}, t_1^{(1)}, p^{(1)}, q^{(1)})$, $(w^{(3)}, t_1^{(1)}, p^{(2)}, q^{(1)})$ and $(w^{(3)}, t_1^{(1)}, p^{(1)}, q^{(2)})$ are shown in Fig. 2a, and the surface quality of them is better than the specimens of Salehghaffari et al. [37], Mokhtarnezhad et al. [38] and Darvizeh, et al. [40] obviously. All grooved tubes were put on the bottom stainless steel plate of a 30-ton SUNS UTM5000 microcomputer controlled electronic universal testing machine without any additional constrains. To eliminate the mechanical clearance, a preloading with a force of 10 N was exerted on each specimen by a top stainless steel plate of the testing machine. Finally, all specimens were compressed by the top plate with a speed of 1 mm/min until all thin-walled sections were collapsed completely.

3.2. Material properties

The mechanical properties of aluminum 2A12 were measured by uni-axial tensile tests. Three identical "dog-bone" specimens were cut from the raw circular tube walls along the axial direction, and the geometric dimensions is shown in Fig. 2b. To measure the linear strain of gauge length accurately, a calibrated extensometer was used (Fig. 2b). The tensile tests were also carried out by using the 30-ton SUNS UTM5000 microcomputer controlled electronic universal testing machine with a speed of 1 mm/min. Neglecting the effect of temperature, the true stress-strain relationship is displayed in Fig. 2b by averaging the results of three identical specimens. The detailed material parameters of aluminum 2A12 are listed in Table 2.

4. Numerical model

The explicit time integration version of commercially available finite element (FE) software ABAQUS/Explicit was used to expand the content of the experiments. In this study, an axisymmetric modeling method can be used, because both boundary and geometric conditions of the system are symmetrical about tube axis.

As shown in Fig. 3, the meridional planes of GGT, top and bottom plates are modeled numerically. Especially, both the top and bottom plate of testing machine are simulated by rigid plates. The 4-node bilinear axisymmetric stress elements (CAX4R) were used to modeled the grooved tube, and the 2-node linear axisymmetric discrete rigid elements (RAX2) were used to modeled the top and bottom plates. To ensure the accuracy of simulation results, the global mesh size of system was set to 0.2 mm. For condition $(w^{(3)}, t_1^{(1)}, p^{(1)}, q^{(2)})$ shown in Fig. 3, 8605 CAX4R elements and 40 RAX2 elements are required respectively for the numerical model, which means the amounts of elements is far

Table 5
Buckling modes of thickness gradient conditions obtained by simulation results.

Parameter (mm, mm, mm, mm)	Buckling Mode	Parameter (mm, mm, mm, mm)	Buckling Mode	Parameter (mm, mm, mm, mm)	Buckling Mode
$(w^{(1)}, t_1^{(1)}, p^{(1)}, q^{(1)})$	RAB	$(w^{(2)}, t_1^{(1)}, p^{(1)}, q^{(1)})$	RAB	$(w^{(3)}, t_1^{(1)}, p^{(1)}, q^{(1)})$	RAB
$(w^{(1)}, t_1^{(1)}, p^{(1)}, q^{(2)})$	SAB	$(w^{(2)}, t_1^{(1)}, p^{(1)}, q^{(2)})$	SAB	$(w^{(3)}, t_1^{(1)}, p^{(1)}, q^{(2)})$	SAB
$(w^{(1)}, t_1^{(1)}, p^{(1)}, q^{(3)})$	SAB	$(w^{(2)}, t_1^{(1)}, p^{(1)}, q^{(3)})$	SAB	$(w^{(3)}, t_1^{(1)}, p^{(1)}, q^{(3)})$	SAB

Note: The condition of $q = 0$ mm is viewed as a special type of thickness gradient tube.

less than the numerical model based on three-dimensional solid modeling method with the same accuracy. The elastic parameters of materials (Table 2) and the plastic region of the true stress-strain curve (Fig. 2b) were input into the software directly. Similar to the experimental settings in Section 3.1, there was no need to apply any restraint on the tube, and all DOFs (degree of freedoms) of the bottom rigid plate were constrained. For the top rigid plate, only the DOF along the loading direction (Fig. 3) was not constrained, and a downward displacement was exerted vertically and slowly. To simulate the interactions between the tube and top and bottom plates, the "surface-to-surface" contact algorithm with a friction coefficient of 0.35 [45] were set on the contact surfaces. During the folding process, the self-contact of the tube must be taken into account. The "self-contact" algorithm were set on the inner and outer surfaces of the grooved tube respectively with a friction coefficient of 0.59 [45].

All numerical models were performed on a double 12-core Xeon WS 3.3 GHz with a typical computation time of 2–2.5 h, which was obviously shorter than the time of three-dimensional solid modeling method [39].

5. Results and discussion

5.1. Buckling modes and calibration of mechanical model

Numerical simulation and theory analysis play critical roles in the field of energy absorption, but the results of them must be validated by experiments. Fig. 4a–c display the experiment and simulation results of conditions $(w^{(3)}, t_1^{(1)}, p^{(1)}, q^{(1)})$, $(w^{(3)}, t_1^{(1)}, p^{(2)}, q^{(1)})$ and $(w^{(3)}, t_1^{(1)}, p^{(1)}, q^{(2)})$, respectively. As shown in Fig. 4, the simulation results of force-displacement curves and buckling modes of above conditions are good agreement with that of experiment results, which prove the validity and accuracy of numerical model.

According to Fig. 4, each condition generates six axisymmetric folds at the corresponding thin-walled sections, which causes six obvious peaks in the force-displacement curves. The phenomenon can be explained as follows: At the beginning of folding process of one thin-walled section, the axial load increases significantly due to a result of elastic resistance [37], and then falls significantly because of the formation and rotation of plastic hinges; when all thin-walled sections are collapsed completely, undulating curves are presented in Fig. 4a–c. Although all experiment samples generate perfect axisymmetric folds at

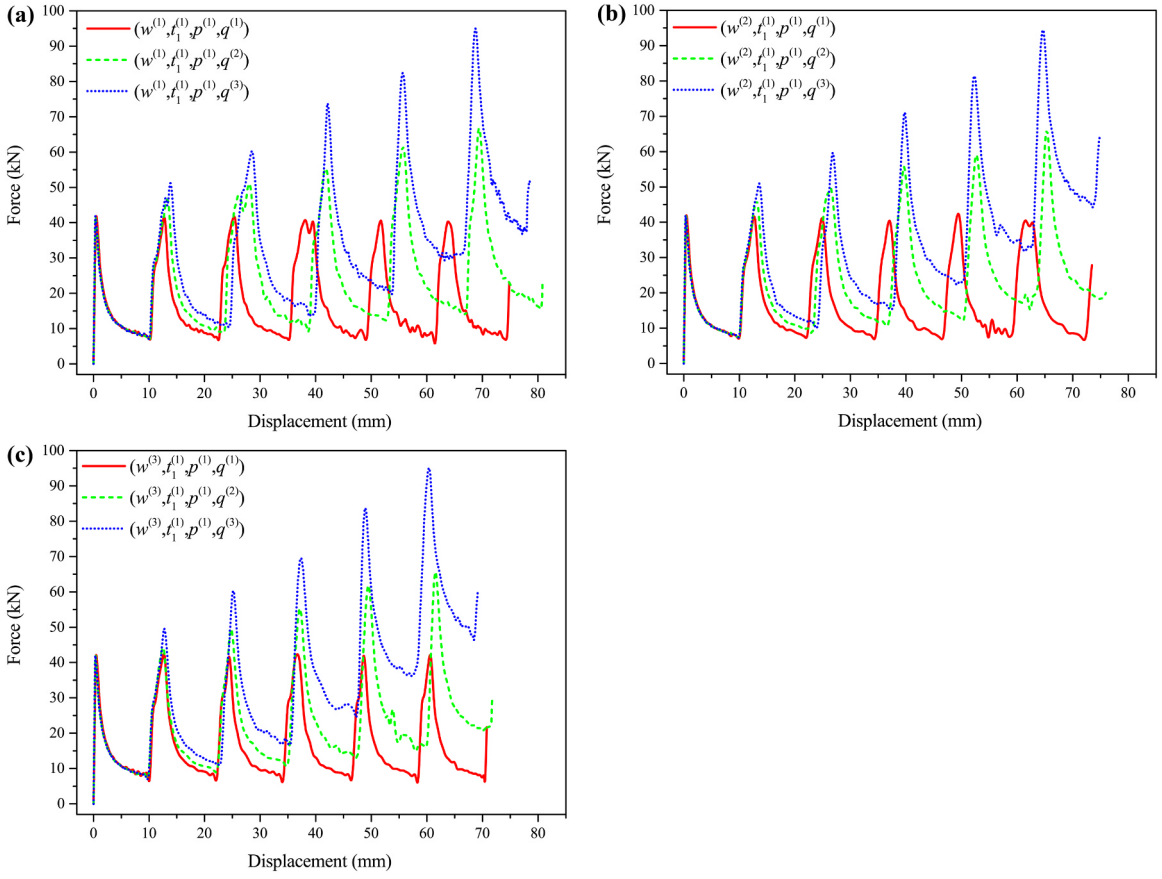

Fig. 8. Typical force-displacement curves of thickness gradient conditions obtained by simulation results: (a) $w = 6.5$ mm; (b) $w = 7.25$ mm; (c) $w = 8$ mm.

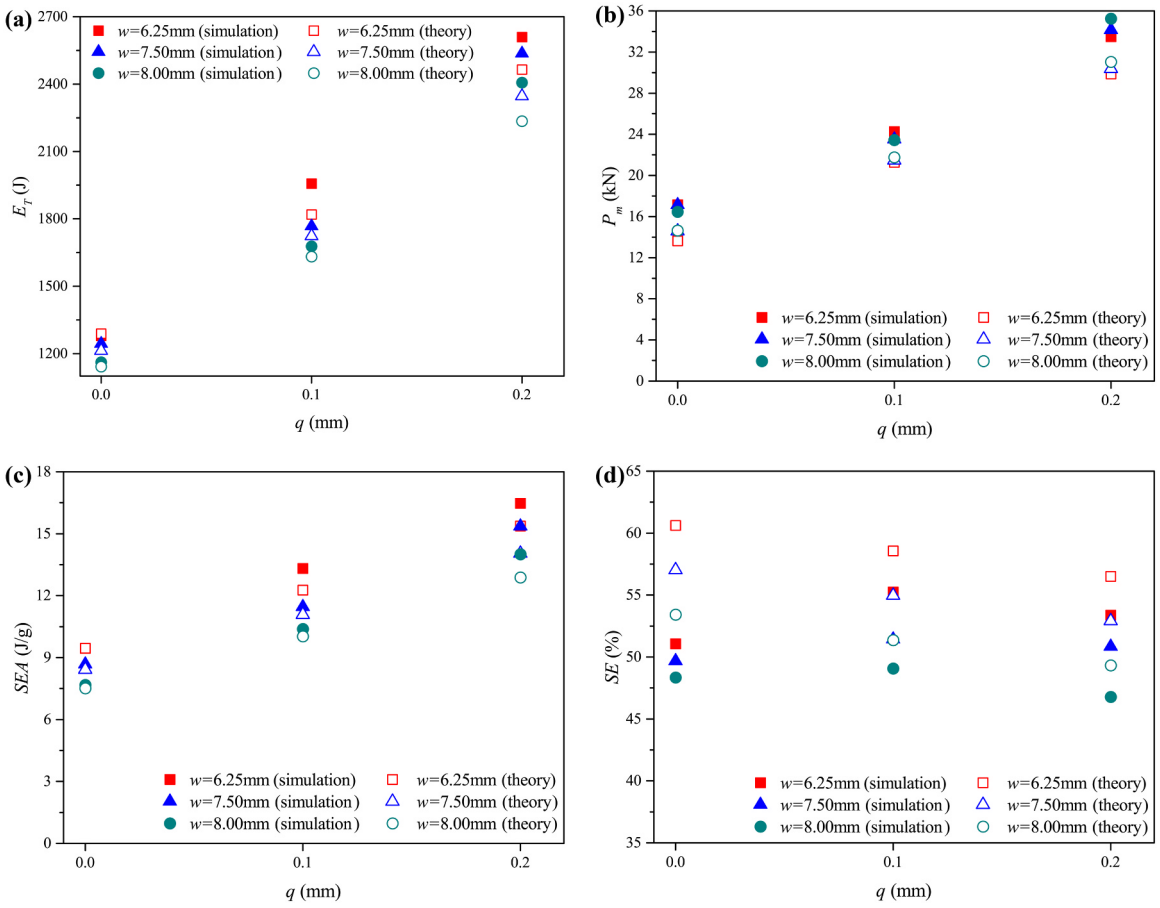

Fig. 9. The simulation and theory results of axial crashworthiness parameters under thickness gradient conditions: (a) E_T; (b) P_m (c) *SEA*; (d) *SE*.

their thin-walled sections, there are still marked differences in the buckling processes. For conditions ($w^{(3)}$, $t_1^{(1)}$, $p^{(1)}$, $q^{(1)}$) (Fig. 4a) and ($w^{(3)}$, $t_1^{(1)}$, $p^{(2)}$, $q^{(1)}$) (Fig. 4b), the buckling sequence of thin-walled sections is uncertain, and the latter fold just starts to form after the former one is generated completely. Refer to the naming methods of buckling modes of the corrugated tube [27], the buckling mode of grooved tube shown in Fig. 4a–b is defined as the random asymptotic buckling (RAB). But for condition ($w^{(3)}$, $t_1^{(1)}$, $p^{(1)}$, $q^{(2)}$), tube buckles from the thinnest thin-walled section located at the loading end to the fixed end progressively, and the latter fold just starts to form after the former one is generated completely. In this research, the buckling mode shown in Fig. 4c is defined as the sequential asymptotic buckling (SAB). From the point view of applications, the SAB is more ideal than RAB, mainly because it can predict the structural responses accurately by input energy and reuse the undamaged parts easily.

The validation of theoretical model can be performed by accurate experiments and a validated numerical model. In this study, a relationship among the normalized parameters P_{mn}/M_{pn}, D_{in}/t_n, and h_n/t_n of a certain thin-walled section is used to validate the theoretical model. Therefore, the comparisons of theory results with simulation results of the third thin-walled section under all loading conditions is shown in Fig. 5, which presents the reliability of theoretical model. The crashworthiness parameters (mentioned in Section 2.2.4) of conditions ($w^{(3)}$, $t_1^{(1)}$, $p^{(1)}$, $q^{(1)}$), ($w^{(3)}$, $t_1^{(1)}$, $p^{(2)}$, $q^{(1)}$) and ($w^{(3)}$, $t_1^{(1)}$, $p^{(1)}$, $q^{(2)}$) are listed in Table 3. It is observed that the errors among the results of experiments, simulations and theory analysis can be controlled in a low range. Hence, the reliability and efficiency of the numerical model and the theoretical model are fully proved in this section.

5.2. Effects of depth gradient on the grooved tube

Nine conditions with $w = 8$ mm, $\sum_{i=1}^{6} h_i = 90$ mm and $q = 0$ mm (Table 4) are designed to investigate the effects of depth gradient on the grooved tube. According to Table 4, all depth gradient conditions generate the RAB, which is consistent with the experiment results discussed in Section 5.1. Typical force-displacement curves of depth gradient conditions are illustrated in Fig. 6. It is found that the thickness of thin-walled sections presents great effects on the energy absorption because the forces significantly increase when t_1 increases from 1 mm to 1.6 mm. Additionally, the forces of depth gradient conditions are promoted slightly when p increases from 0 mm to 2 mm and t_1 is constant. Fig. 7 displays the simulation and theory results of axial crashworthiness parameters. The E_T, P_m and *SEA* significantly increase when t_1 increases from 1.3 mm to 1.6 mm and p is constant, while slightly increase when p increases from 0 mm to 2 mm and t_1 is constant. According to Fig. 7b and d, the errors of P_m and *SE* are larger than other parameters when $t_1 = 1$ mm, mainly because the actual wavelength of a complete fold is less than the depth of a groove when h_n/t_n is large enough. Moreover, E_T (Fig. 7a), P_m (Fig. 7b) and SEA (Fig. 7c) also have larger errors when $t_1 = 1.6$ mm, because the change of the thickness of thin-walled sections is not considered and the coupling effects of stretching and bending are complex when h_n/t_n is small enough.

The energy absorbing characteristics of D-GGT are very similar with that of ribbed tube with different space of rings [30,31]. That is to say, the folding sequence of thin-walled sections is uncertain, and the total energy absorption can be promoted slightly even though the sum of depth of thin-walled sections is constant. Nevertheless, the D-GGT presented in this research has more stable performances, because it rarely generates the non-axisymmetric mode and Euler mode during the

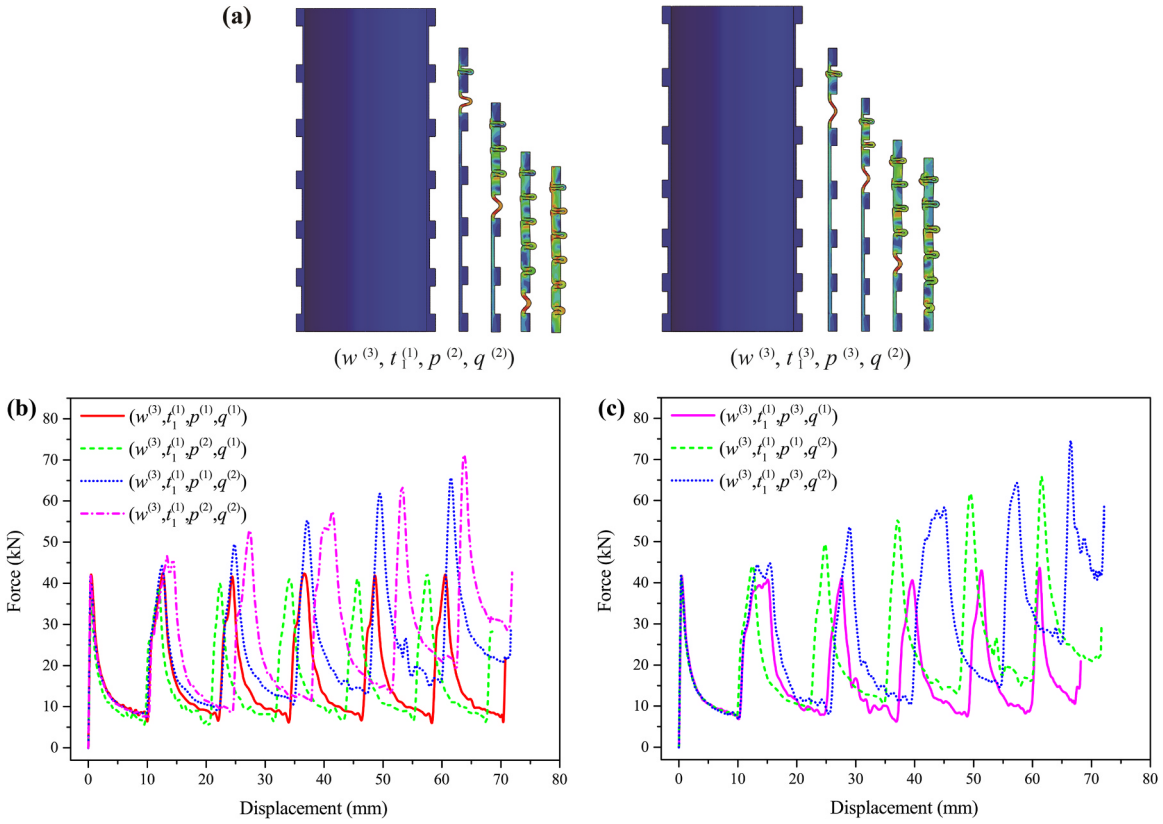

Fig. 10. Typical buckling mode and force-displacement curves of coupling gradient conditions: (a) buckling mode of conditions $(w^{(3)}, t_1^{(1)}, p^{(2)}, q^{(2)})$ and $(w^{(3)}, t_1^{(1)}, p^{(3)}, q^{(2)})$ (sequential asymptotic buckling); (b)-(c) force-displacement curves of coupling gradient condition $(w^{(3)}, t_1^{(1)}, p^{(2)}, q^{(2)})$ and $(w^{(3)}, t_1^{(1)}, p^{(3)}, q^{(2)})$ compared with that of single gradient conditions.

axial compression.

5.3. Effects of thickness gradient on the grooved tube

Nine conditions with $t_1 = 1$ mm and $p = 0$ mm (Table 5) are designed to study the effects of thickness gradient on the grooved tube. According to Table 5, all conditions with $q = 0$ mm generate the RAB, while the SAB only appears on the conditions with $q > 0$ mm. The typical force-displacement curves of thickness gradient conditions are illustrated in Fig. 8a-c. The curves present an obviously upward trend when q increases from 0 mm to 0.2 mm. However, when q is constant, the load among different curves present barely noticeable differences when w increases 6.5–8 mm, and the total compression displacement decreases due to the obvious decrease of $\sum_{i=1}^{N} h_i$. As shown in Fig. 9a–d, the simulation and theory results of axial crashworthiness parameters show a similarly tendency. For conditions with the same w, the E_T, P_m, and *SEA* obviously increases when q increases from 0 mm to 0.2 mm. But for conditions with the same q, parameters slight decrease when w increases 6.5–8 mm due to the decrease of the sum of thin-walled sections. Compared with depth gradient, the thickness gradient has a more significant effect on energy absorption of grooved tube. Additionally, the causes of errors produced by theoretical model have been explained clearly in Section 5.2.

For T-GGT, both the SAB mode and a force-displacement curve with obvious upward trend can be obtained because the structural stiffness is increased stage by stage along the axial direction of the tube. Actually, the similar results of buckling mode and force-displacement curve also can be obtained from the tapered tube with or without thickness gradient [46,47] and functionally-grade structures [48]. Nevertheless, the T-GGT has two obvious advantages compared with them: one is the easy processing; the other is the certainty of deformation zone, which brings great convenience for theoretical analysis and numerical simulation.

5.4. Effects of coupling gradient on the grooved tube

The axial buckling modes and the crashworthiness performance of D-GGT and T-GGT tube have been thoroughly investigated in Sections 5.1, 5.2 and 5.3, respectively. In this section, the grooved tube with both depth and thickness gradients is proposed, and two coupling gradient conditions $(w^{(3)}, t_1^{(1)}, p^{(2)}, q^{(2)})$ and $(w^{(3)}, t_1^{(1)}, p^{(3)}, q^{(2)})$ are designed to investigate the buckling mode and axial crushing performance numerically. According to Fig. 10a, tubes buckle from the deepest and thinnest thin-walled section located at the loading end to the fixed end progressively, which means the C-GGT always generates the SAB mode. Comparisons between the typical force-displacement curves of coupling gradient condition and single gradient conditions are shown in Fig. 10b-c. The force-displacement curves of coupling gradient conditions tend to shift backwards compared with that of single gradient conditions, and the curves also show a slightly ascending trend compared with that of thickness gradient conditions, thus the coupling gradient conditions have larger E_T, P_m and *SEA*. In fact, this phenomenon can be explained by the normalized mean crashing force of one thin-walled section (Fig. 11): compared with the single gradient condition, the P_{mn}/M_{pn} of coupling gradient condition increases slightly when the gradual decrease of h_n/t_n.

As discussed above, the C-GGT always generates the SAB mode mainly because of the arrangement of thickness gradient, while the slight improvement of energy absorption compared with the T-GGT is attributed to the depth gradient. Therefore, it can be predicted that C-GGT contains the energy absorption characteristics of D-GGT and T-GGT simultaneously.

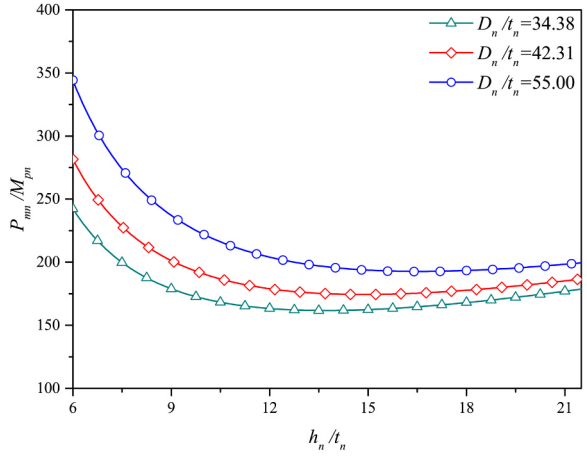

Fig. 11. Normalized mean crashing force of the nth thin-walled section with h_n/t_n and D_n/t_n obtained by theory results.

6. Conclusions

In this research, the axial buckling modes and crashworthiness of circular tube with external linear gradient grooves are investigated theoretically, experimentally and numerically. The following conclusions may be drawn:

(1) A theoretical model considering both the depth and thickness gradients and a novel numerical model tube based on axisymmetric assumption for grooved tube are proposed. The reliability of the theoretical and numerical models is validated by a series of accurate experiments.
(2) The deformation of GGT under axial buckling can be classified into two modes, namely, the random asymptotic buckling (RAB) and sequential asymptotic buckling (SAB). During the axial compression, the UGT ($p = 0$, $q = 0$) and D-GGT ($p \neq 0$, $q = 0$) always generate the RAB mode, while the T-GGT ($p = 0$, $q \neq 0$) and C-GGT ($p \neq 0$, $q \neq 0$) generate the SAB mode more easily
(3) The axial energy performance of GGT is investigated by comparing with that of UGT. For D-GGT, the axial crashworthiness can be improved slightly even though the sum of depth of thin-walled sections is constant; for T-GGT, a significant improvement of energy absorption performance and a force-displacement curve with obvious upward trend are observed; for C-GGT, both the energy absorption characteristics of D-GGT and T-GGT will occur.

Acknowledgments

This work is supported by Traffic Scientific Research Project of Shaanxi Province Transportation Department, China (13-16k); Chang'an University's Undergraduate Training Programs, China for Innovation and Entrepreneurship (201810710139); and Chang'an University's Innovation and Open Laboratory Project, China (2018CXSY06). The authors would like to gratefully acknowledge Bei Zhang for writing MATLAB programs, Hai-ming Liu and Ya-guang Huo for machining specimens.

References

[1] N. Jones, Structural Impact, Cambridge University Press, Cambridge, UK, 2011.
[2] C. Bisagni, Crashworthiness of helicopter subfloor structures, Int. J. Impact Eng. 27 (10) (2002) 1067–1082.
[3] Z. Ahmad, D.P. Thambiratnam, Application of foam-filled conical tubes in enhancing the crashworthiness performance of vehicle protective structures, Int. J. Crashworthiness 14 (4) (2009) 349–363.
[4] L.L. Hu, T.X. Yu, Z.Y. Gao, X.Q. Huang, The inhomogeneous deformation of polycarbonate circular honeycombs under in-plane compression, Int. J. Mech. Sci. 50 (7) (2008) 1224–1236.
[5] A. Baroutaji, M. Sajjia, A.G. Olabi, On the crashworthiness performance of thin-walled energy absorbers: recent advances and future developments, Thin-Walled Struct. 118 (2017) 137–163.
[6] S. Ramakrishna, H. Hamada, Energy absorption characteristics of crash worthy structural composite materials, Key Eng. Mater. 141–143 (143) (1998) 585–622.
[7] S. Palanivelu, W.V. Paepegem, J. Degrieck, J. Vantomme, D. Kakogiannis, J.V. Ackeren, et al., Crushing and energy absorption performance of different geometrical shapes of small-scale glass/polyester composite tubes under quasi-static loading conditions, Compos Struct. 93 (2) (2011) 992–1007.
[8] R.M. Sampaio, C.L. Sales, On the effect of geometrical designs and failure modes in composite axial crushing: a literature review, Compos Struct. 94 (3) (2012) 803–812.
[9] A. Atthapreyangkul, B.G. Prusty, Experimental and numerical analysis on the geometrical parameters towards the maximum SEA of CFRP Components, Compos Struct. 164 (2017) 229–236.
[10] G.X. Lu, T.X. Yu, Energy Absorption of Structures and Materials, Woodhead Publishing Limited, Cambridge, 2003.
[11] A.G. Mamalis, M. Robinson, D.E. Manolakos, G.A. Demosthenous, M.B. Ioannidis, J. Carruthers, Crashworthy capability of composite material structures, Compos. Struct. 37 (2) (1997) 109–134.
[12] A.G. Mamalis, D.E. Manolakos, M.B. Ioannidis, D.P. Papapostolou, On the experimental investigation of crash energy absorption in laminate splaying collapse mode of FRP tubular components, Compos. Struct. 70 (4) (2005) 413–429.
[13] L.N.S. Chiu, B.G. Falzon, R. Dong, S. Xu, R.S. Thomson, B. Chen, et al., Crush responses of composite cylinder under quasi-static and dynamic loading, Compos. Struct. 131 (2015) 90–98.
[14] A.A.A. Alghamdi, Collapsible impact energy absorbers: an overview, Thin-Walled Struct. 39 (2) (2001) 189–213.
[15] X.M. Qiu, T.X. Yu, Some topics in recent advances and applications of structural impact dynamics, Appl. Mech. Rev. 38 (64) (2011) 4001.
[16] S.R. Guillow, G. Lu, R.H. Grzebieta, Quasi-static axial compression of thin-walled circular aluminium tubes, Int. J. Mech. Sci. 43 (2001) 2103–2123.
[17] J.M. Alexander, An approximate analysis of the collapse of thin cylindrical shells under axial loading, Q. J. Mech. Appl. Math. 13 (1) (1960) 10–15.
[18] K.R.F. Andrews, G.L. England, E. Ghani, Classification of the axial collapse of cylindrical tubes under quasi-static loading, Int. J. Mech. Sci. 25 (9) (1983) 687–696.
[19] T. Wierzbicki, S.U. Bhat, W. Abramowicz, D. Brodkin, Alexander revisited-A two folding elements model of progressive crushing of tubes, Int. J. Solids Struct. 29 (24) (1992) 3269–3288.
[20] A.A. Singace, H. Elsobky, T.Y. Reddy, On the eccentricity factor in the progressive crushing of tubes, Int. J. Solids Struct. 32 (24) (1995) 3589–3602.
[21] A.A. Singace, H. Elsobky, Further experimental investigation on the eccentricity factor in the progressive crushing of tubes, Int. J. Solids Struct. 33 (24) (1996) 3517–3538.
[22] H. Han, J. Cheng, F. Taheri, N. Pegg, Numerical and experimental investigations of the response of aluminum cylinders with a cutout subject to axial compression, Thin-Walled Struct. 44 (2) (2006) 254–270.
[23] H. Han, F. Taheri, N. Pegg, Quasi-static and dynamic crushing behaviors of aluminum and steel tubes with a cutout, Thin-Walled Struct. 45 (3) (2007) 283–300.
[24] H. Yılmaz, İ. Kocabaş, E. Özyurt, Empirical equations to estimate non-linear collapse of medium-length cylindrical shells with circular cutouts, Thin-Walled Struct. 119 (2017) 868–878.
[25] A.A. Singace, H. Elsobky, Behaviour of axially crushed corrugated tubes, Int. J. Mech. Sci. 39 (3) (1997) 249–268.
[26] A. Eyvazian, M.K. Habibi, A.M. Hamouda, R. Hedayati, Axial crushing behavior and energy absorption efficiency of corrugated tubes, Mater. Des. 54 (2) (2014) 1028–1038.
[27] Z.F. Liu, W.Q. Hao, J.M. Xie, J.S. Lu, R. Huang, Z.H. Wang, Axial-impact buckling modes and energy absorption properties of thin-walled corrugated tubes with sinusoidal patterns, Thin-Walled Struct. 94 (2015) 410–423.
[28] W.Q. Hao, J.M. Xie, F.H. Wang, Theoretical prediction of the progressive buckling and energy absorption of the sinusoidal corrugated tube subjected to axial crushing, Comput. Struct. 191 (2017) 12–21.
[29] W.Q. Hao, J.M. Xie, F.H. Wang, Z.F. Liu, Z.H. Wang, Analytical model of thin-walled corrugated tubes with sinusoidal patterns under axial impacting, Int. J. Mech. Sci. 128–129 (2017) 1–16.
[30] T. Adachi, A. Tomiyama, W. Araki, A. Yamaji, Energy absorption of a thin-walled cylinder with ribs subjected to axial impact, Int. J. Impact Eng. 35 (2) (2008) 65–79.
[31] C.W. Isaac, O. Oluwole, Energy absorption improvement of circular tubes with externally press-fitted ring around tube surface subjected under axial and oblique impact loading, Thin-Walled Struct. 109 (C) (2016) 352–366.
[32] Y. Wei, Z. Yang, H. Yan, Y. Guo, X. Wu, C. Huang, Proactive regulation of axial crushing behavior of thin-walled circular tube by gradient grooves, Int. J. Mech. Sci. 108–109 (2016) 49–60.
[33] A.G. Mamalis, G.L. Viegelahn, D.E. Manolakos, W. Johnson, Experimental investigation into the axial plastic collapse of steel thin-walled grooved tubes, Int. J. Impact Eng. 4 (2) (1986) 117–126.
[34] A.G. Mamalis, D.E. Manolakos, G.L. Viegelahn, N.M. Vaxevanidis, W. Johnson, The inextensional collapse of grooved thin-walled cylinders of PVC under axial loading, Int. J. Impact Eng. 4 (1) (1986) 41–56.
[35] S.J. Hosseinipour, G.H. Daneshi, Energy absorbtion and mean crushing load of thin-walled grooved tubes under axial compression, Thin-Walled Struct. 41 (1) (2003) 31–46.
[36] S.J. Hosseinipour, Mathematical model for thin-walled grooved tubes under axial compression, Mater. Des. 24 (6) (2003) 463–469.
[37] S. Salehghaffari, M. Tajdari, M. Panahi, F. Mokhtarnezhad, Attempts to improve

energy absorption characteristics of circular metal tubes subjected to axial loading, Steel Constr. 48 (6) (2010) 379–390.
[38] F. Mokhtarnezhad, S. Salehghaffari, M. Tajdari, Improving the crashworthiness characteristics of cylindrical tubes subjected to axial compression by cutting wide grooves from their outer surface, Int. J. Crashworthiness 14 (6) (2009) 601–611.
[39] S. Salehghaffari, M. Rais-Rohani, A. Najafi, Analysis and optimization of externally stiffened crush tubes, Thin-Walled Struct. 49 (3) (2011) 397–408.
[40] A. Darvizeh, A. Meshkinzar, M. Alitavoli, R. Rajabiehfard, Low velocity impact of empty and foam filled circumferentially grooved thick-walled circular tubes, Thin-Walled Struct. 110 (2017) 97–105.
[41] Z. Yang, Y. Yu, Y. Wei, C. Huang, Crushing behavior of a thin-walled circular tube with internal gradient grooves fabricated by SLM 3D printing, Thin-Walled Struct. 111 (2017) 1–8.
[42] C. Zhou, S. Ming, C. Xia, B. Wang, X. Bi, P. Hao, et al., The energy absorption of rectangular and slotted windowed tubes under axial crushing, Int. J. Mech. Sci. 141 (2018) 89–100.
[43] A.G. Hanssen, M. Langseth, O.S. Hopperstad, Static and dynamic crushing of square aluminium extrusions with aluminium foam filler, Int. J. Impact Eng. 24 (5) (1999) 475–507.
[44] X. Zhang, K. Leng, H. Zhang, Axial crushing of embedded multi-cell tubes, Int. J. Mech. Sci. 131–132 (2017) 459–470.
[45] D.T. Qin, L.Y. Xie, Modern Handbook of Mechanical Design, Chemical Press, Beijing, China, 2011.
[46] X. Zhang, H. Zhang, Z. Wen, Axial crushing of tapered circular tubes with graded thickness, Int. J. Mech. Sci. 92 (2015) 12–23.
[47] D. Meric, H. Gedikli, Energy absorption behavior of tailor-welded tapered tubes under axial impact loading using coupled FEM/SPH method, Thin-Walled Struct. 104 (2016) 17–33.
[48] G. Li, Z. Zhang, G. Sun, X. Huang, Q. Li, Comparison of functionally-graded structures under multiple loading angles, Thin-Walled Struct. 94 (2015) 334–347.